

Supporting Information

Tuning intermediates adsorption for efficient electrosynthesis of urea from carbon dioxide and nitrate via doping Au into Cu

Yangfan Song,[#] Yong Zhang,[#] Xinyi Yang, Yiran Guo, Meiqin Xu, Guozhu Gao,
Feifei Chen, Weihua Wang, Feng Lu, Hong Dong,* Hui Liu,* and Yahui Cheng*

*Department of Electronic Science and Engineering and Tianjin Key Laboratory of Process Control
and Green Technology for Pharmaceutical Industry, Nankai University, Tianjin 300350, China*

[#]Yangfan Song and Yong Zhang contributed equally to this work.

** Corresponding author: Hong Dong (donghong@nankai.edu.cn); Hui Liu
(liuhui@nankai.edu.cn); Yahui Cheng (chengyahui@nankai.edu.cn)*

Details of the experimental methods

1. Electrochemical test

The electrolyte solution for both the anode and cathode was prepared using a mixture of 0.5 M KHCO₃ and 0.05 M KNO₃. Prior to the tests, CO₂ gas was continuously bubbled through the cathode electrolyte for 10 min. Electrochemical measurements were conducted under a constant potential mode (-0.3, -0.4, -0.5, -0.6, and -0.7 V vs. RHE). The scan rate for linear sweep voltammetry (LSV) testing is set to 5 mV s⁻¹. The potentials applied in experiments were transformed into the RHE scale following the equation below:

$$E(\text{vs.RHE}) = E(\text{vs.Ag/AgCl}) + 0.197 \text{ V} + 0.059 \text{ V} \times Ph \quad (1)$$

Following 15 min of continuous electrolysis, the urea in the catholyte was determined using diacetyl monoxime reagent or hydrogen nuclear magnetic resonance (¹H-NMR) spectroscopy. Indophenol blue spectrophotometry and ion chromatography (IC) were employed for the quantitative detection of NH₃ and NO₂⁻, respectively. Gas chromatography (GC) was used to analyze the potential gaseous by-products CO. Isotope labeling experiments and *in situ* Raman measurements were conducted using the same methods.

2. Determination of urea

For the detection of urea: First, dissolve diacetylmonoxime (400 mg) and thiosemicarbazide (8 mg) in 80 mL of deionized water to obtain solution A. Then, add ferric chloride (8 mg), concentrated phosphoric acid (8 mL) and concentrated sulfuric acid (24 mL) sequentially to 48 mL of deionized water to obtain solution B. Next, add solution A (2 mL) and B (2 mL) to 1 mL of cathodic electrolyte to form the solution C. Heat the solution C to 100 °C in boiling water for 20 min, and then allow it to cool to room temperature. After cooling, measure the UV-vis absorption spectrum of the solution C, recording the absorbance at 525 nm.

3. Determination of NH₃

For the detection of NH₃: First, dissolve Sodium salicylate (4.16 g) sodium citrate (4.74 g) and NaOH (3.20 g) in 80 mL of deionized water to get solution 1. Second, 2.8

mL of NaClO (6 ~ 15%) was diluted in 77.2 mL of deionized water to get solution 2. Third, dissolve Sodium nitroferricyanide (0.4 g) in 20 mL of deionized water to get solution 3. Next, add solution 1 (2.4 mL), solution 2 (0.4 mL) and solution 3 (1.8 mL) cathodic electrolyte to form the solution 4. After allowing solution 4 to stand in the dark at room temperature for 60 ~ 120 min, the absorbance at 670 nm was measured using UV-Vis absorption spectroscopy.

The FE for urea, NH_3 , NO_2^- , and CO can be calculated using the following formulas:

$$FE_{\text{urea}}(\%) = \frac{16 \times F \times c_{\text{urea}} \times V}{60.06 \times Q} \times 100\% \quad (1)$$

$$FE_{\text{NH}_3}(\%) = \frac{8 \times F \times c_{\text{NH}_3} \times V}{17 \times Q} \times 100\% \quad (2)$$

$$FE_{\text{NO}_2^-}(\%) = \frac{2 \times F \times c_{\text{NO}_2^-} \times V}{46 \times Q} \times 100\% \quad (3)$$

$$FE_{\text{CO}}(\%) = \frac{2 \times F \times c_{\text{CO}} \times V}{46 \times Q} \times 100\% \quad (4)$$

Here, c_{urea} , c_{NH_3} , $c_{\text{NO}_2^-}$ and c_{CO} (ppm) are the concentrations of the measured urea, NH_3 , NO_2^- and CO, respectively; F is the Faraday constant (96485 C mol^{-1}), V (mL) stands for the total amount of electrolyte solution, and Q (C) signifies the accumulated charge passing through the working electrode. The numbers 16, 8, 2, and 2 represent the number of electrons required to form one molecule of urea, NH_3 , NO_2^- , and CO, respectively.

The following equation was used to calculate the yield rate of urea:

$$R_{\text{urea}} = \frac{c_{\text{urea}} \times V}{t \times A}, \quad (5)$$

where t is the time (h) for electrocatalysis and A is the catalyst geometric area (cm).

4. DFT Computational details

All the DFT calculations were performed using the Vienna ab initio simulation package (VASP 5.4.4), employing the PAW method and PBE functional to calculate and simulate ion-electron interactions and exchange-correlation energy. A four-layer 2×2 supercell of Cu (111) was constructed, with a Cu atom on the surface replaced by an Au atom to represent the Cu-Au catalyst. A 25 Å vacuum layer was added along the

z-direction to adsorb reactants and prevent interactions between periodic structures. The *k*-point mesh for the Brillouin zone was set to $2 \times 2 \times 1$, with a cutoff energy of 400 eV. The convergence criteria were set to 0.05 eV \AA^{-1} for force and 10^{-5} eV for energy.

The Gibbs free energy (ΔG) can be expressed as:

$$\Delta G = \Delta E + \Delta ZPE - T \times \Delta S, \quad (6)$$

ΔE represents the reaction energy obtained using DFT calculations, while ΔZPE and $T \times \Delta S$ denote the thermodynamic corrections for the zero-point energy (ZPE) and entropy (S) calculated via the vibrational partition function at 298.15 K.

The Nudged Elastic Band (NEB) method,¹ which enables the determination of the minimum energy path between reactants, intermediates, and products, was used to evaluate the value of energy barriers. The climbing image NEB (CI-NEB) method was applied to a discretized path of 5 images.² We calculated the reaction barrier as the difference between the saddle points and reactants. All the atoms of intermediate NEB images are relaxed, while atomic structures of the reactants and products are permanently fixed in NEB calculations. Frequency calculations were applied to verify the adsorbed intermediates and the transition states (with only one imaginary frequency).

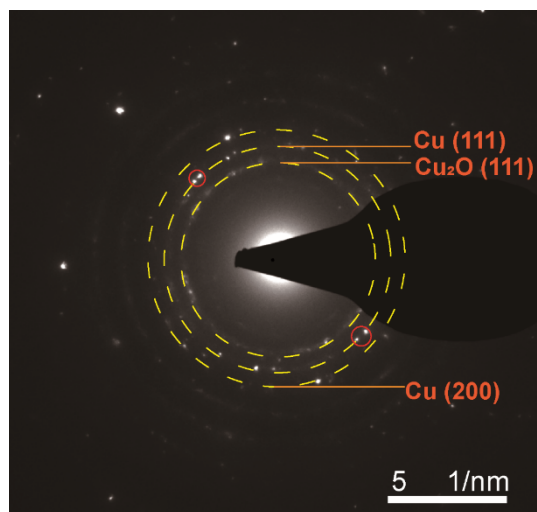


Fig. S1. Selected area electron diffraction (SAED) image of Cu-Au.

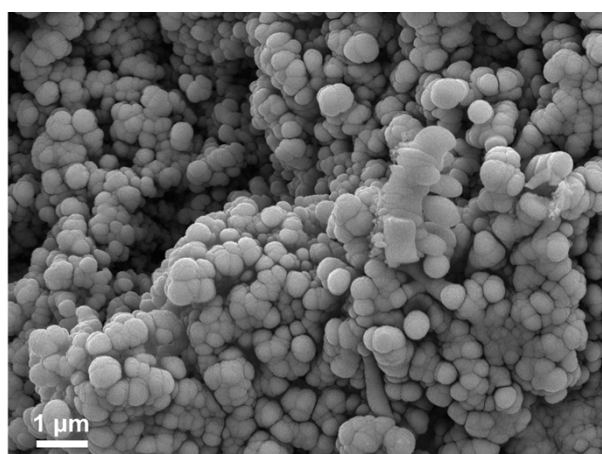


Fig. S2. SEM image of the Cu catalyst.

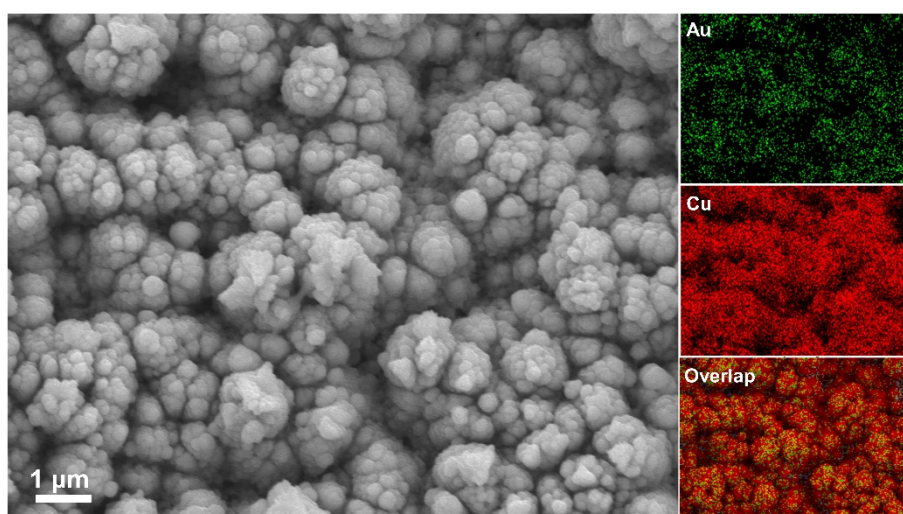


Fig. S3. SEM image of the Cu-Au catalyst and corresponding energy-dispersive X-ray (EDX) elemental mappings.

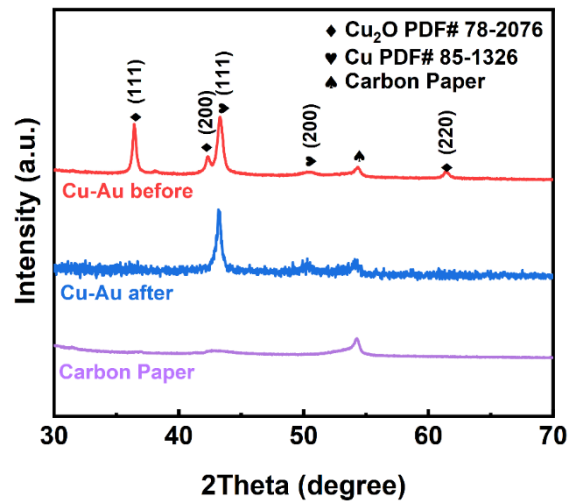


Fig. S4. XRD patterns of Cu-Au catalyst before and after electrolysis, carbon paper.

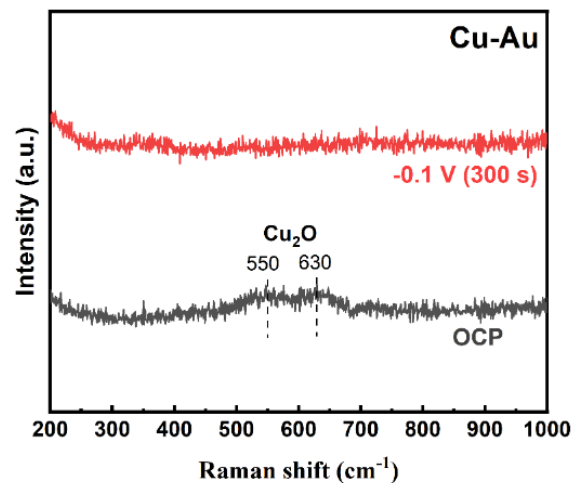


Fig. S5. In-situ Raman spectra of Cu-Au in CO_2 -saturated electrolyte solution at -0.1 V for 300 s.

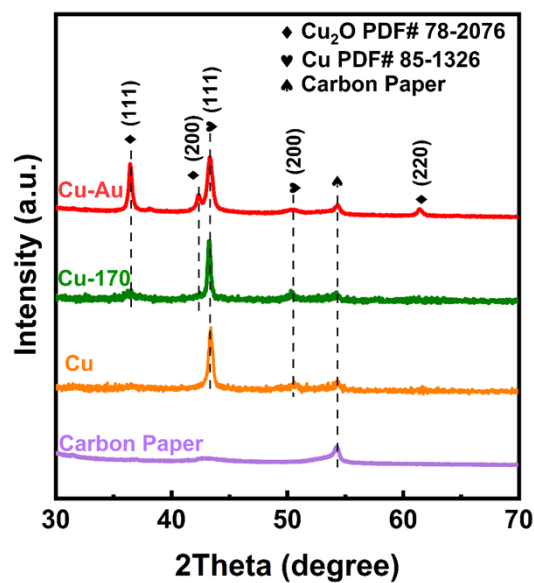


Fig. S6. XRD pattern of Cu-Au catalyst, Cu-170 catalyst, Cu catalyst, and carbon paper.

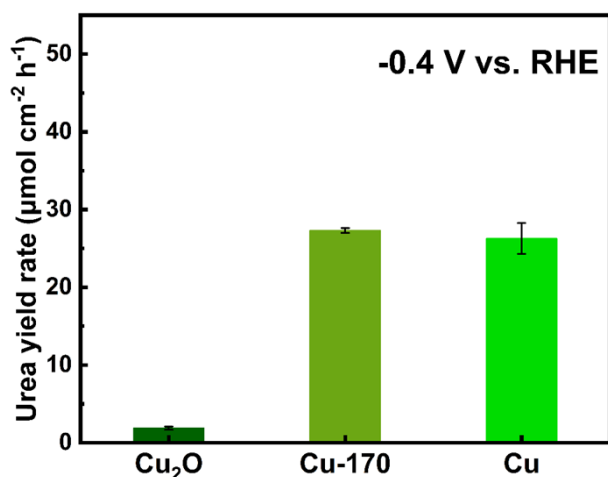


Fig. S7. Urea yield rate of Cu_2O , Cu-170 and Cu.

To investigate whether the electrocatalytic activity of the catalysts originates from surface oxide components, Cu catalyst was annealed in air at 170 °C for 1 hour, yielding Cu-170 catalyst, which exhibits a Cu_2O peak in its XRD pattern as shown in Fig. S6. Urea yield rates of Cu, Cu-170, and Cu_2O catalysts at optimal potential (-0.4 V vs. RHE) were measured using UV-vis absorption spectra. As depicted in Fig. S7, there was nearly no difference in urea catalytic performance between Cu-170 and Cu catalysts, while the urea yield rate on the Cu_2O catalyst was negligible. It indicates that the excellent electrocatalytic activity of the Cu-Au catalyst is unlikely to originate from surface oxide components.

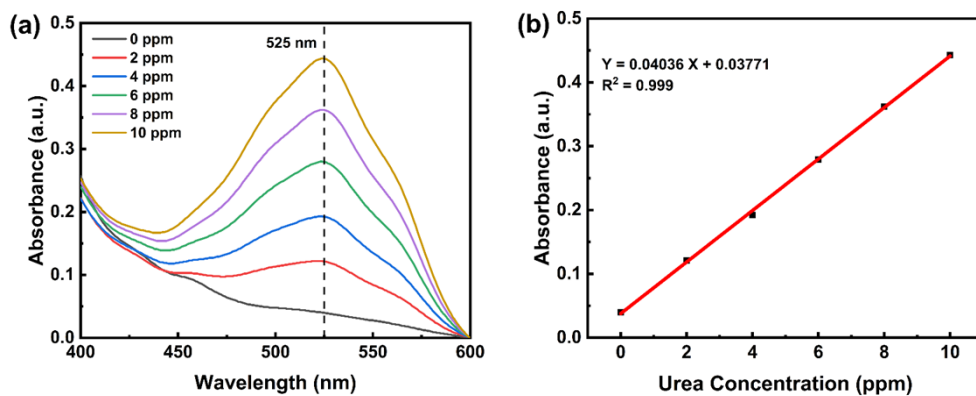


Fig. S8. (a) UV-vis absorption spectra and (b) calibration curves of urea. Absolute calibration was performed using a range of urea solutions of known concentration as standards.

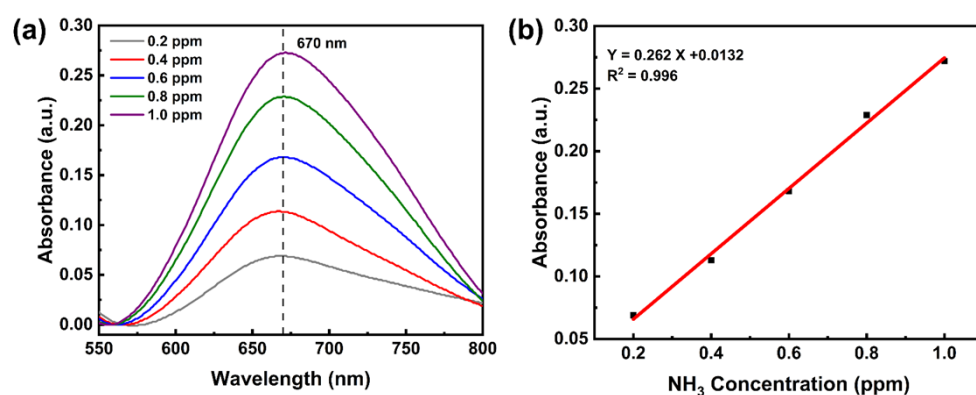


Fig. S9. (a) UV-vis absorption spectra and (b) calibration curves of NH_3 . Absolute calibration was performed using a range of NH_3 solutions with known concentration as standards.

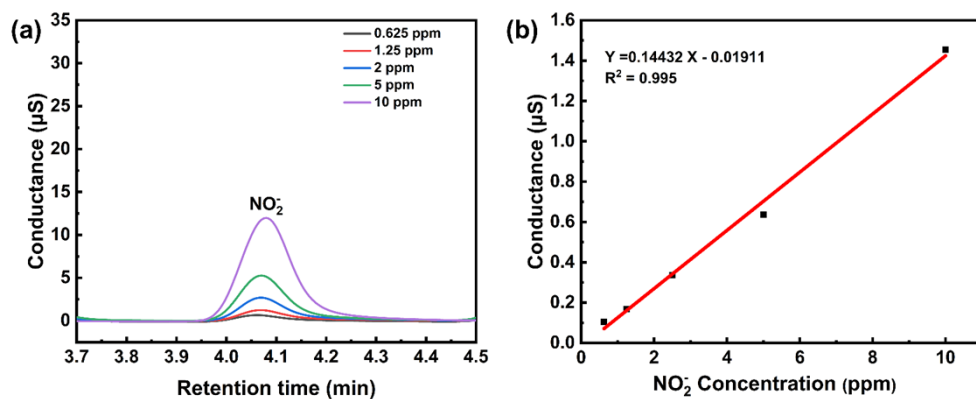


Fig. S10. (a) spectra of ion chromatography and (b) calibration curves of NO_2^- . Absolute calibration was performed using a range of NO_2^- solutions with known concentration as standards.

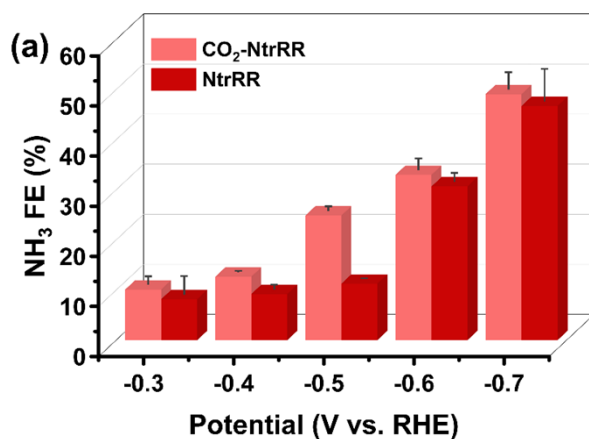


Fig. S11. NH₃ Faradaic efficiency of the NO₃⁻ reduction reaction (NtrRR) and CO₂ and NO₃⁻ co-reduction reaction (CO₂-NtrRR) over the Cu-Au catalyst.

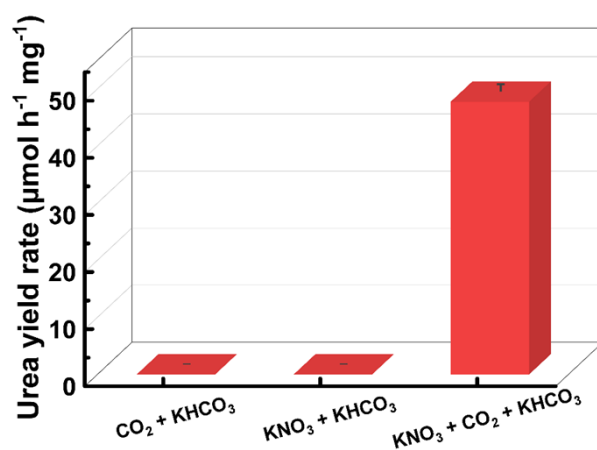


Fig. S12. Urea synthesis under various conditions in 0.5 M KHCO₃.

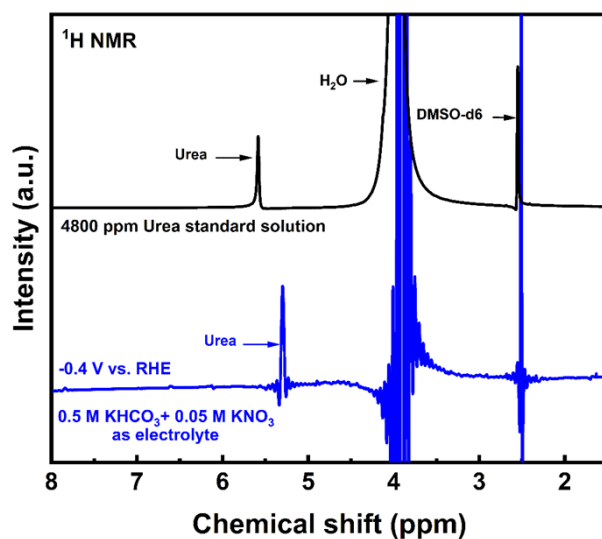


Fig. S13. ¹H NMR spectra of urea standard solution and urea produced via 0.5 M KHCO₃ + 0.05 M KNO₃ with CO₂ saturated on Cu-Au at -0.4 V vs. RHE.

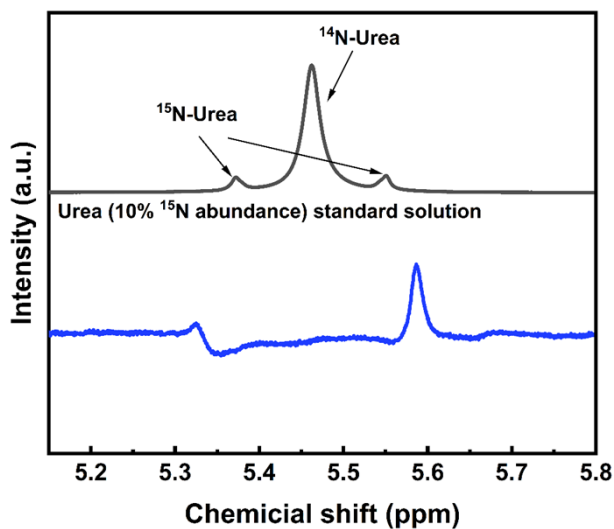


Fig. S14. ^1H NMR spectra of urea standard sample with 10% abundance of ^{15}N and urea produced via $0.5\text{ M KHCO}_3 + 0.05\text{ M K}^{15}\text{NO}_3$ with CO_2 saturated on Cu-Au at -0.4 V vs. RHE.

In Fig. S14, the asymmetry of the double peak is mainly caused by the water inhibition model during testing, and the positions of the double peaks are basically the same as those of urea (10% ^{15}N abundance) standard solution.

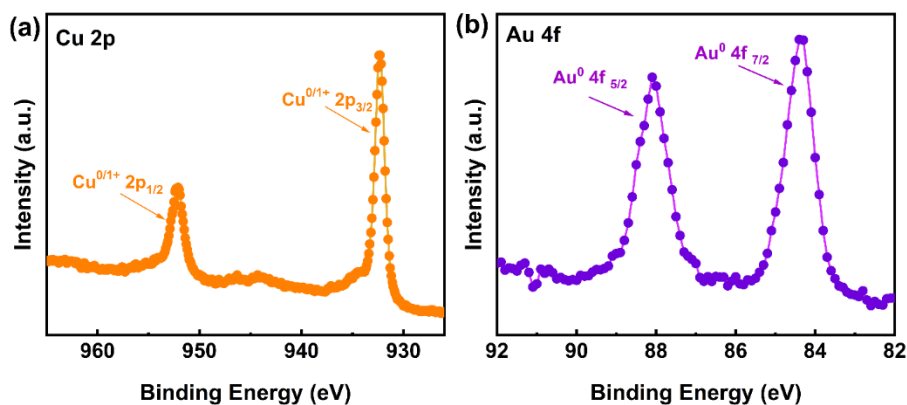


Fig. S15. XPS spectra of the Cu-Au catalyst after electrolysis.

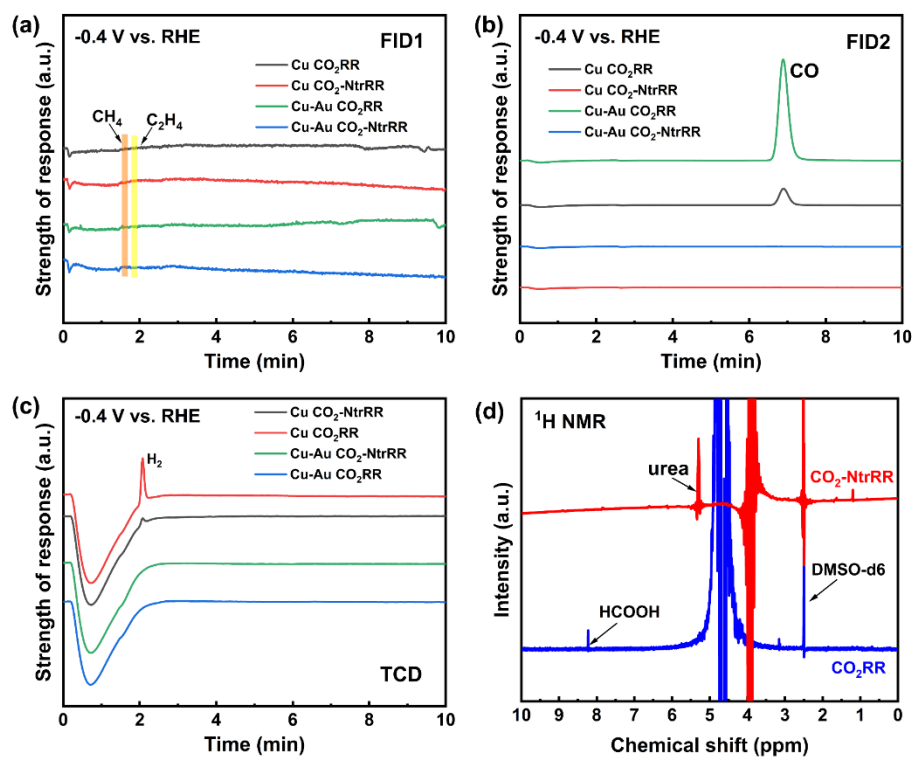


Fig. S16. The gas chromatograms of (a) FID1, (b) FID2, and (c) TCD of Cu-Au and Cu catalysts after CO₂RR and CO₂-NtrRR and (d) ¹H NMR spectra of electrolyte after the CO₂ and NO₃⁻ co-reduction and CO₂RR over Cu-Au catalyst at -0.4 V.

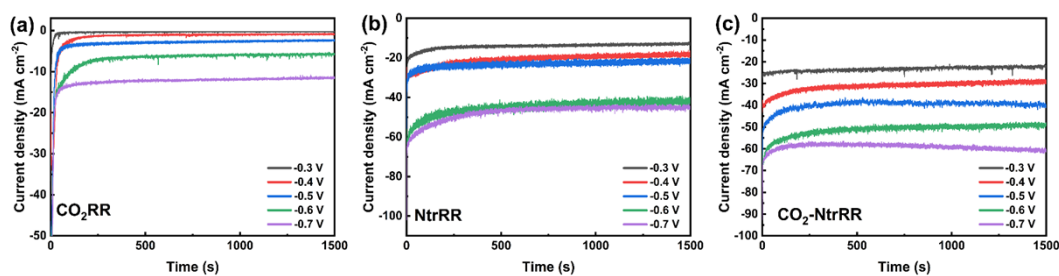


Fig. S17. Cu-Au catalyst electrolysis in (a) 0.5 M KHCO₃ with CO₂ saturated, (b) 0.5 M KHCO₃ + 0.05 M KNO₃ and (c) 0.5 M KHCO₃ + 0.05 M KNO₃ with CO₂ saturated at potential range from -0.3 V to -0.7 V vs. RHE for 1500 seconds.

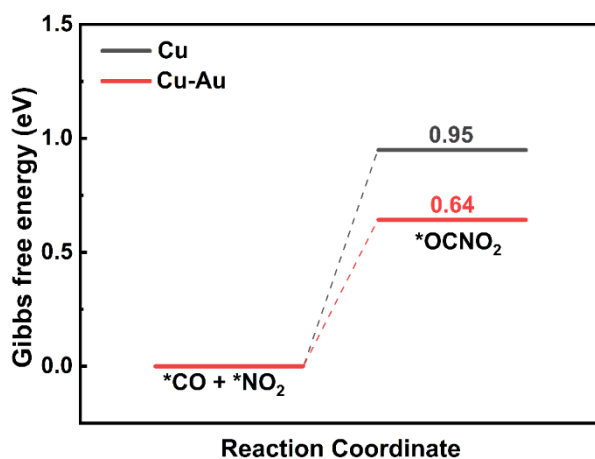


Fig. S18. Reaction energies of *CO-*NO₂ coupling over Cu and Cu-Au surface.

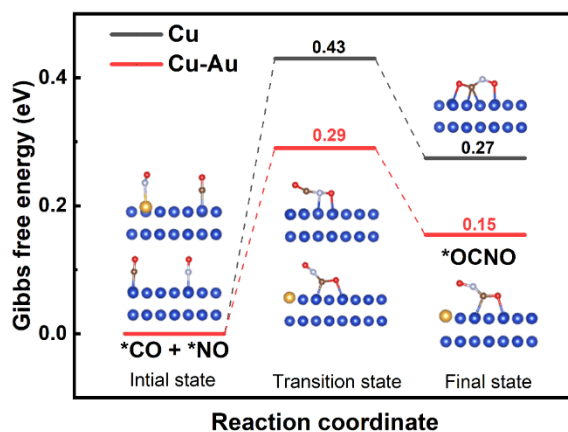


Fig. S19. Transition state calculations of C-N coupling over Cu (111) and Cu-Au surface.

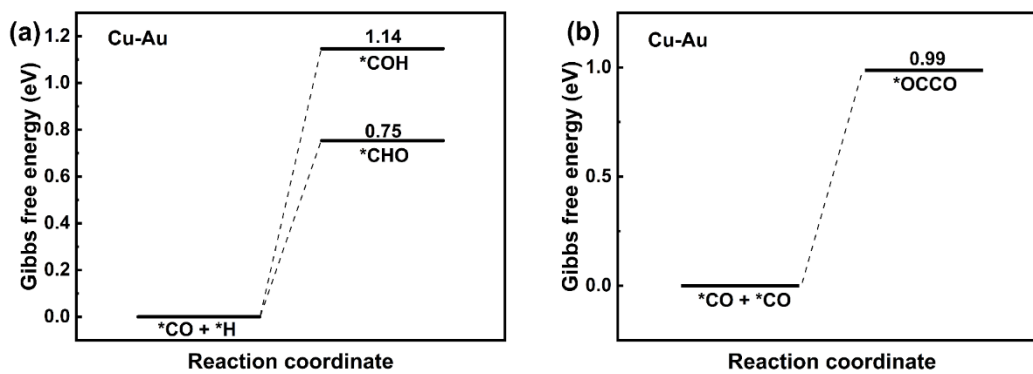


Fig. S20. Reaction energies for (a) $*CO$ hydrogenation to form $*CHO$ and $*COH$ intermediates and (b) dimerization of $*CO$ on the Cu-Au surface.

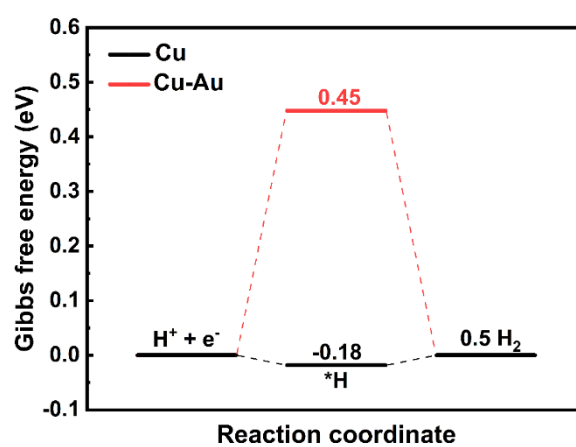


Fig. S21. Reaction energies for HER over Cu and Cu-Au surface.

Table S1 Surface concentrations of elements (atomic percent) on the Cu-Au catalyst derived from XPS.

Catalyst	Cu (at%)	Au (at%)
Cu-Au	98.1	1.9

Table S2 ICP-OES measurements for the Cu-Au catalyst.

Catalyst	Solution Cu concentration (ppm)	Solution Au concentration (ppm)	Cu (at%)	Au (at%)
Cu-Au	120	3	99.2	0.8

The ICP-OES sample preparation method included cutting the GDE with deposited catalyst into 0.25 cm² square, adding 1 mL of aqua regia, and standing for 30 min until the Cu and Au on the GDE surface were completely dissolved. Finally, the 1 mL aqua regia was diluted to 1000 mL for ICP-OES measurements.

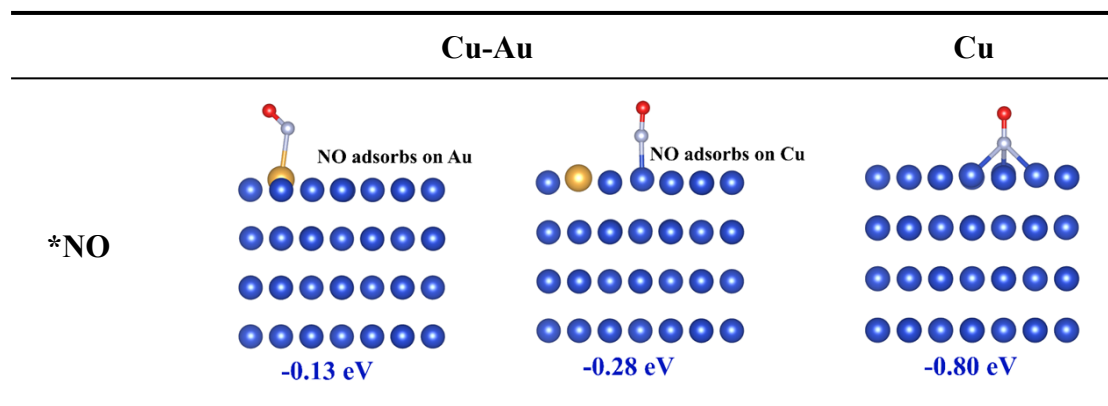
Table S3 Electrocatalytic performance of coupling CO₂ and oxynitride to urea in previous reports.

Catalyst	Electrolyte	Reactants	Optimal potential (V vs. RHE)	FE (%)	Ref.
Cu-Au	0.5 M KHCO₃ 0.05 M KNO₃	CO₂, NO₃⁻	-0.4	67.81	This work
Cu-GS	0.1 M KHCO ₃ 0.1 M KNO ₃	CO ₂ , NO ₃ ⁻	-0.9	28	3
Cu@Zn	0.2 M KHCO ₃ 0.1 M KNO ₃	CO ₂ , NO ₃ ⁻	-1.02	9.28	4
NC	0.1 M KHCO ₃ 0.1 M KNO ₃	CO ₂ , NO ₃ ⁻	-0.5	62	5
Cu ₉₉ Ni ₁	0.1 M KHCO ₃ 0.02 M KNO ₂	CO ₂ , NO ₂ ⁻	-0.7	39.8	6
AuPd	75 mM KHCO ₃ 25 mM KNO ₃	CO ₂ , NO ₃ ⁻	-0.65	15.6	7
ZnO-V	0.2 M NaHCO ₃ 0.1 M NaNO ₂	CO ₂ , NO ₂ ⁻	-0.79	23.26	8
F-CNT	0.1 M KNO ₃	CO ₂ , NO ₃ ⁻	-0.65	18	9
MoO _x /C	0.1 M KNO ₃	CO ₂ , NO ₃ ⁻	-0.6	27.7	10
Bi: 10%In/C	0.1 M KHCO ₃ 0.1 M KNO ₃	CO ₂ , NO ₃ ⁻	-0.45	20.31	11
c-Cu ₂ O	0.1 M KHCO ₃ 0.05 M NaNO ₃	CO ₂ , NO ₃ ⁻	-1.5	17.7	12
RhCu-uls	0.1 M KNO ₃	CO ₂ , NO ₃ ⁻	-0.6	34.82	13
GB-rich Bi	0.1 M KNO ₃	CO ₂ , NO ₃ ⁻	-0.4	32	14

Table S4 Surface concentrations of elements (atomic percent) on the Cu-Au catalyst derived from XPS before and after reduction.

Cu-Au	Cu (at%)	Au (at%)
Before reduction	98.1	1.9
After reduction	98.2	1.8

Table S5 Optimized adsorption structure and adsorption energy of *NO intermediate involved in the co-reduction process of Cu-Au and bare Cu catalysts.



References

1. Mills, G., Jónsson, H. & Schenter, G. K. Reversible work transition state theory: application to dissociative adsorption of hydrogen. *Surf. Sci.*, 1995, **324**, 305-337.
2. Henkelman, G., Uberuaga, B. P. & Jónsson, H. A climbing image nudged elastic band method for finding saddle points and minimum energy paths. *J Chem. Phys.*, 2000, **113**, 9901-9904.
3. J. Leverett, T. Tran-Phu, J.A. Yuwono, P. Kumar, C. Kim, Q. Zhai, C. Han, J. Qu, J. Cairney, A.N. Simonov, R.K. Hocking, L. Dai, R. Daiyan, R. Amal, Tuning the coordination structure of Cu-N-C single atom catalysts for simultaneous electrochemical reduction of CO₂ and NO₃⁻ to urea, *Adv. Energy Mater.*, 2022, **12**(32), 2201500.
4. N. Meng, Y. Huang, Y. Liu, Y. Yu, B. Zhang, Electrosynthesis of urea from nitrite and CO₂ over oxygen vacancy-rich ZnO porous nanosheets, *Cell Rep. Phys. Sci.*, 2021, **2**(3), 100378.
5. Y. Zhang, Y. Zhao, M.G. Sendeku, F. Li, J. Fang, Y. Wang, Z. Zhuang, Y. Kuang, B. Liu, X. Sun, Tuning intermediates adsorption and C-N coupling for efficient urea electrosynthesis via doping Ni into Cu, *Small Methods*, 2023, **8**(3), 2300811.
6. N. Meng, X. Ma, C. Wang, Y. Wang, R. Yang, J. Shao, Y. Huang, Y. Xu, B. Zhang, Y. Yu, Oxide-derived core-shell Cu@Zn nanowires for urea electrosynthesis from carbon dioxide and nitrate in water, *ACS Nano*, 2022, **16**(6), 9095-9104.
7. Y. Li, S. Zheng, H. Liu, Q. Xiong, H. Yi, H. Yang, Z. Mei, Q. Zhao, Z. Yin, M. Huang, Y. Lin, W. Lai, S. Dou, F. Pan, S. Li, Sequential co-reduction of nitrate and carbon dioxide enables selective urea electrosynthesis, *Nat. Commun.*, 2024, **15**(1), 176.
8. H. Wang, Y. Jiang, S. Li, F. Gou, X. Liu, Y. Jiang, W. Luo, W. Shen, R. He, M. Li, Realizing efficient C-N coupling via electrochemical co-reduction of CO₂ and NO₃⁻ on AuPd nanoalloy to form urea: key C-N coupling intermediates, *Appl. Catal., B.*, 2022, **318**, 121819.
9. X. Liu, P.V. Kumar, Q. Chen, L. Zhao, F. Ye, X. Ma, D. Liu, X. Chen, L. Dai, C. Hu, Carbon nanotubes with fluorine-rich surface as metal-free electrocatalyst for effective synthesis of urea from nitrate and CO₂, *Appl. Catal., B*, 2022, **316**, 121618.
10. M. Sun, G. Wu, J. Jiang, Y. Yang, A. Du, L. Dai, X. Mao, Q. Qin, Carbon-anchored molybdenum oxide nanoclusters as efficient catalysts for the electrosynthesis of ammonia and urea, *Angew. Chem. Int. Ed.*, 2023, **62**(19), 202301957.

11. Y. Mao, Y. Jiang, Q. Gou, S. Lv, Z. Song, Y. Jiang, W. Wang, M. Li, L. Zheng, W. Su, R. He, Indium-activated bismuth-based catalysts for efficient electrocatalytic synthesis of urea, *Appl. Catal., B*, 2024, **340**, e202301957.
12. J. Zhao, Y. Yuan, F. Zhao, W. Han, Q. Yuan, M. Kou, J. Zhao, C. Chen, S. Wang, Identifying the facet-dependent active sites of Cu₂O for selective C-N coupling toward electrocatalytic urea synthesis, *Appl. Catal., B*, 2024, **340**, 123265.
13. S. Fu, K. Chu, M. Guo, Z. Wu, Y. Wang, J. Yang, F. Lai, T. Liu, Ultrasonic-assisted hydrothermal synthesis of RhCu alloy nanospheres for electrocatalytic urea production, *Chem. Commun.*, 2023, **59**(29), 4344-4347.
14. Y. Wang, S. Xia, R. Cai, J. Zhang, C. Yu, J. Cui, Y. Zhang, J. Wu, Y. Wu, Dynamic reconstruction of two-dimensional defective Bi nanosheets for efficient electrocatalytic urea synthesis, *Angew. Chem. Int. Ed.*, 2024, **63**(16), e202318589.